Chemical Geology 467 (2017) 159–167

Contents lists available at ScienceDirect

Chemical Geology

journal homepage: www.elsevier.com/locate/chemgeo

# Anomalous mercury enrichment in Early Cambrian black shales of South China: Mercury isotopes indicate a seawater source

Runsheng Yin[a,b,*], Lingang Xu[c], Bernd Lehmann[d], Ryan F. Lepak[b], James P. Hurley[b], Jingwen Mao[e], Xinbin Feng[f], Ruizhong Hu[a]

[a] State Key Laboratory of Ore Deposit Geochemistry, Institute of Geochemistry, Chinese Academy of Sciences, Guiyang 550002, China
[b] Environmental Chemistry and Technology Program, University of Wisconsin-Madison, Madison, WI, 53706, USA
[c] State Key Laboratory of Geological Processes and Mineral Resources, China University of Geosciences, Beijing 100083, China
[d] Mineral Resources, Technical University of Clausthal, 38678 Clausthal-Zellerfeld, Germany
[e] MLR Key Laboratory of Metallogeny and Mineral Assessment, Institute of Mineral Resources, Chinese Academy of Geological Sciences, Beijing 100037, China
[f] State Key Laboratory of Environmental Geochemistry, Institute of Geochemistry, Chinese Academy of Sciences, Guiyang 550002, China

ARTICLE INFO

*Keywords:*
Early Cambrian
Sulfide-rich black shale
Seawater
Hg isotopes

ABSTRACT

Extremely elevated Hg levels up to the μg $g^{-1}$ range were found in sulfide-rich black shale and phosphorite in the lowermost part of the Early Cambrian black shale sequences on the Yangtze Platform in South China. In this study, mercury isotopes were used to help resolve the origin of this anomalous Hg enrichment. Mass independent fractionation signatures of Hg isotopes with positive $\Delta^{199}$Hg values of 0.13 to 0.24‰ and positive $\Delta^{200}$Hg values of 0.05 to 0.10‰ were observed, indicating seawater is an important source of Hg. We hypothesize that upwelling of nutrient-rich waters from the open ocean resulted in high bioproductivity in the photic zone with concomitant scavenging of Hg from seawater. Advanced decay of biomass and remineralization under anoxic to euxinic conditions combined with very low clastic input led to enrichment of Hg and a broad spectrum of other redox-sensitive and biogenic metals up to $10^7$ compared to modern seawater. Such spectacular hydrogenous metal enrichment has previously been observed in the oxic deep-sea environment only, i.e. manganese crusts/nodules.

## 1. Introduction

Black shales are widespread at the Precambrian/Cambrian transition and document a global ocean anoxic event, which is part of major environmental and biological changes, such as plate tectonic reconfiguration, mass extinction, and accelerated diversification of metazoans (Kimura and Watanabe, 2001; Steiner et al., 2001). The southeast margin of the Yangtze Platform in South China has extensive exposures of Early Cambrian black shale sequences (Niutitang Formation and equivalents). These black shales represent a condensed transgressive shelf sequence which rests with a slight unconformity on the rifted margin of the Late Neoproterozoic Yangtze carbonate platform (Wang et al., 2012a). The lowermost part of the Niutitang black shale hosts economic deposits of phosphorite, barite, sapropelic alginite (combustible shale, “stone coal”) and an unusual polymetallic sulfide-rich black shale unit (Fig. 1). This shale unit exhibits an extreme enrichment of a broad metal spectrum (Ni-Mo-Au-As-Zn-Se and others). Although the polymetallic sulfide-rich shales have been known since about 40 years, their origin remains much debated with opposing models: (1) hydrothermal seafloor venting (Steiner et al., 2001; Jiang et al., 2006, 2007; Pašava et al., 2010) versus (2) scavenging from seawater by organic matter (Mao et al., 2002; Lehmann et al., 2007, 2016; Xu et al., 2011, 2013).

Mercury (Hg) may be used as a proxy to understand the formation of the polymetallic sulfide-rich shales. The Early Cambrian black shale sequence of the Niutitang Formation has > $10^4$ times enrichment in Hg, when compared to the upper continental crust (Lehmann et al., 2007; Taylor and McLennan, 1995). Organic matter (OM) has a high affinity to Hg (Grasby et al., 2013), and Hg concentrations have been used as an indicator to understand the origin of several mass extinction events (Sanei et al., 2012; Sial et al., 2013, 2016; Thibodeau et al., 2016; Grasby et al., 2017). Hg stable isotope geochemistry offers new insights into the sources and geochemical processes of Hg (Bergquist and Blum, 2009; Blum et al., 2014). Mercury is comprised of seven stable isotopes (196–204 amu), which are subject to both mass-dependent fractionation (MDF) and mass-independent fractionation (MIF). MDF (reported as $\delta^{202}$Hg) has been observed during various abiotic/biotic Hg transformations, whereas MIF of odd isotopes (reported as

* Corresponding author.
*E-mail address:* yinrunsheng@mail.gyig.ac.cn (R. Yin).

http://dx.doi.org/10.1016/j.chemgeo.2017.08.010
Received 14 March 2017; Received in revised form 30 July 2017; Accepted 9 August 2017
Available online 12 August 2017

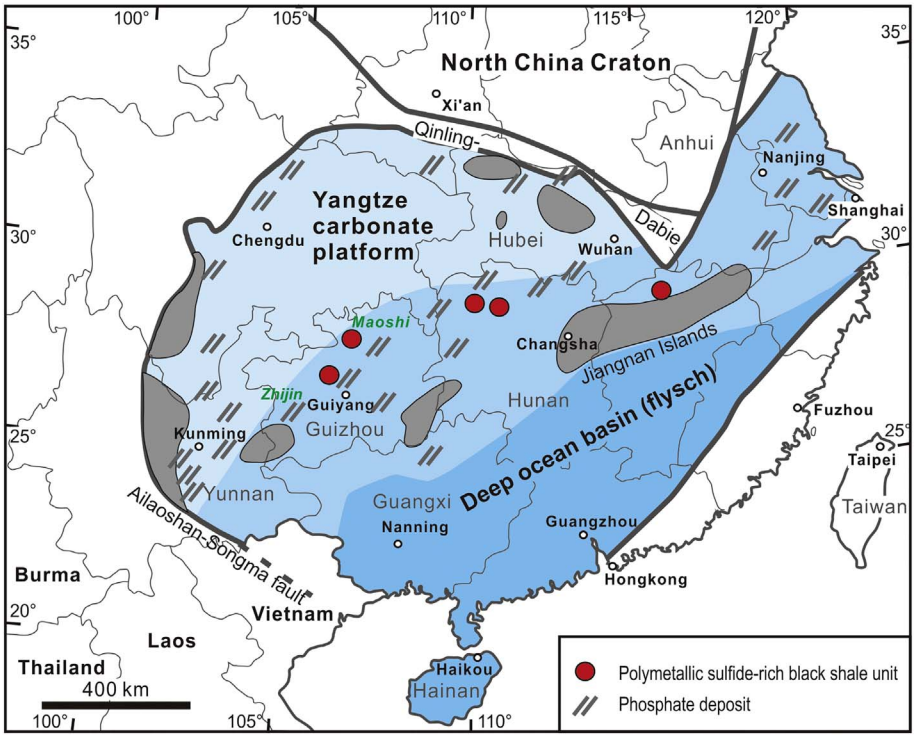


**Fig. 1.** Sketch map showing the location of the Maoshi polymetallic sulfide-rich black shale unit and the Zhijin phosphorite deposit. Paleogeographic reconstruction indicates that the Early Cambrian is characterized by a marine transgression on the Late Neoproterozoic carbonate platform with a heavily condensed stratigraphic succession of black shale. Gray shaded areas are paleoislands. The area between the Yangtze carbonate platform (very light blue) and the deep-sea basin (blue) is marginal shallow Yangtze Sea and shown in light blue (modified from Lehmann et al., 2016). (For interpretation of the references to colour in this figure legend, the reader is referred to the web version of this article.)

$\Delta^{199}$Hg and $\Delta^{201}$Hg) has been observed during only a few processes (Bergquist and Blum, 2007, 2009; Zheng and Hintelmann, 2009; Blum et al., 2014). Large variations of ~10‰ for $\Delta^{199}$Hg and $\Delta^{201}$Hg values were reported among different source materials on Earth (Blum et al., 2014). Photochemical reactions (e.g., aqueous Hg(II) photoreduction, MeHg photodegradation) may be of global importance to the observed MIF (Sonke, 2011; Blum et al., 2014). In recent years, small MIF of ~1‰ for even isotopes (reported as $\Delta^{200}$Hg and $\Delta^{204}$Hg) was reported, likely linked to atmospheric Hg(0) photo-oxidation because even-mass MIF is mainly observed in atmospheric samples (Gratz et al., 2010; Chen et al., 2012; Sun et al., 2016). Overall, combining "MDF-MIF" of Hg isotopes can provide multi-dimensional information about sources and geochemical fates of Hg in the environment.

Here, we report anomalously high Hg levels in Early Cambrian polymetallic sulfide-rich black shale (Maoshi site) and phosphorite (Zhijin site) in South China. Using Hg isotope tracers, we present a model for the specific paleoenvironmental conditions responsible for Hg (and other redox-sensitive metal) enrichment in the Early Cambrian marine sedimentary record.

## 2. Geological setting

Neoproterozoic and Early Cambrian marine sedimentary rocks are well exposed on the Yangtze Platform, South China, and have been paleogeographically recognized as a regional depositional zone with a shallow shelf facies (carbonate platform) in the northwest to a transitional and deep basinal facies of black shale and chert in the southeast (Zhu et al., 2003; Wallis, 2007) (Fig. 1). Both the polymetallic Ni-Mo-sulfide-rich black shale and phosphorite units occur discontinuously over a strike length of > 1500 km in the basal Early Cambrian Niutitang Formation (and equivalent formations), a few meters above the low-angle unconformity of the Late Neoproterozoic (Ediacaran) dolomite of the Dengying Formation. Based on comparison of more than twenty sections from the carbonate platform to the southeastward deep basin, Zhu et al. (2003) identified a segmented offshore basin situation at the transitional zone which was separated to the deep basin by carbonate seamounts. A restricted environment in the offshore basins at the transition zone of the Yangtze platform is documented by variable thickness of the Dengying Formation and the Niutitang Formation. The rate of sedimentation in some units of the restricted basins, such as the polymetallic Ni-Mo-sulfide-rich sediments, was several hundred times slower than that of modern euxinic sediments, e.g. Black Sea and Cariaco Basin (Lehmann et al., 2007), and underlines the existence of sediment starved restricted basins. The polymetallic Ni-Mo-sulfide-rich layer is in the NE-trending belt of transitional shelf facies, whereas the phosphorite layer is both in the transitional shelf and the relatively shallower carbonate platform margin facies (Jiang et al., 2007; Xu et al., 2013; Lehmann et al., 2016). The black shales of the Niutitang Formation are several tens of meters thick, with abundant marine fossils of a wide biological diversity that mark the "Cambrian Explosion" (Steiner et al., 2001). The detailed stratigraphy of the Niutitang Formation has been described by Xu et al. (2013).

The polymetallic Ni-Mo-sulfide layer is a few centimeters thick, and contains rip-up clasts of pyrite, phosphorite and a phase composed mainly of Mo, S, and C and referred to as MoSC (Kao et al., 2001).The peculiar MoSC component together with Ni sulfides and bituminous matter of high thermal maturation stage correspond to the very-low-grade metamorphic history of the Niutitang Formation (Kříbek et al., 2007). Phosphorite concretions are abundant below and in the polymetallic Ni-Mo sulfide layer, and grade to massive phosphorite where no polymetallic Ni-Mo sulfide marker unit occurs, indicating that the polymetallic Ni-Mo sulfide unit and the phosphorite unit are lateral equivalents. Re-Os dating indicates that the polymetallic sulfide-rich black shale was deposited at 521 ± 5 Ma (Xu et al., 2011), well correlated with the zircon U-Pb age of 522.7 ± 4.9 Ma of a thin tuff layer that locally occurs just below the phosphorite layer (Wang et al., 2012b).

## 3. Analytical methods

### 3.1. Sample collection and preparation

We examined two Early Cambrian black shale units from two mine sites in Guizhou, SW China: (1) the polymetallic sulfide-rich black shale

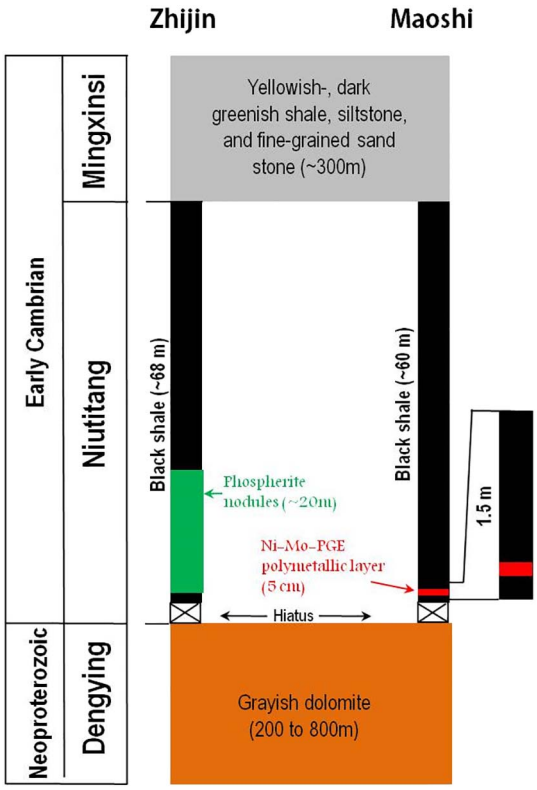


**Fig. 2.** Stratigraphic column showing the Neoproterozoic–Early Cambrian sedimentary sequences of the area studied.

at Maoshi (N: 27°49′, E: 106°46′), and (2) the Zhijin phosphorite deposit (N: 26°35′, E: 105°52′). These sites are typical of many other occurrences of metal-rich black shale and phosphorite along the 1500 km along Early Cambrian paleo-margin of the Yangtze Platform (Fig. 1). The samples from the Maoshi section are focused on the 10 cm-thick polymetallic sulfide-rich black shale unit which is mined for Mo and Ni (two samples), and the underlying and overlying black shale (3 black shale samples below the ore unit, each at 10 cm stratigraphic interval; 5 black shale samples above the ore unit, each at 20 cm stratigraphic interval) (Fig. 2). The sampling section of the Zhijin phosphorite deposit spans the entire Niutitang Formation with a stratigraphic thickness of about 60 m, and includes the 20 m-thick lower unit of phosphorite (5 samples) and the overlying 40 m-thick black shale (15 samples) (Fig. 2). We took fresh bulk samples of 0.5 to 1 kg weight, which were crushed, and powdered with an agate shatter box, prior to chemical analysis.

### 3.2. Elemental concentration analysis

Phosphorus pentoxide ($P_2O_5$), total organic carbon (TOC), Mo and S composition were measured at the Chinese National Research Center of Geoanalysis in Beijing. $P_2O_5$ analysis was done using an ICP-AES (PE8300) instrument. Samples were prepared and dissolved using aqua regia, and subsequently analyzed in a batch system. The aqua regia digestion allows complete dissolution of the sulfide component, and avoids the complex matrix which would result from the usual HF-$HNO_3$ digestion. Each sample batch contains a method reagent blank, a certified reference material, and sample duplicates. The uncertainty is below 5% for ICP-AES analysis. Mo content was determined using an ICP-MS (X-series) instrument. The reagent blanks were treated following the same procedures as the samples. Total analytical errors for Mo in this study are within ± 6% (1 σ). TOC was analyzed using the potassium dichromate method (Schumacher, 2002). Organic matter in samples was oxidized to $CO_2$ in potassium dichromate solution. Contents of TOC were calculated according to potassium dichromate consumption. Sulfur composition was measured by infrared C-S analyzer (Bédard et al., 2008). Samples were oxidized in a high-temperature furnace to transform sulfur into $SO_2$ gas. The total sulfur content was calculated according to the content of collected $SO_2$. The precision of both TOC and S analyses was < 1%. Total Hg concentrations of rock powder samples were measured using a direct combustion system (Nippon MA-2) followed by atomic absorption spectroscopy analysis at the USGS-Wisconsin Mercury Research Laboratory (Olund, 2004). Measurements of standard reference material (IAEA SL 1) showed recoveries of 91 and 110%, and coefficients of variation for triplicate analyses were < 6%.

### 3.3. Mercury isotope analysis

Hg isotopic compositions were measured by the Neptune Plus MC-ICP-MS instrument at the Wisconsin State Laboratory of Hygiene using methods detailed previously (Lepak et al., 2015; Yin et al., 2016). Specifically, about 0.2 g of ground sample was digested (95 °C, 1 h) in 2.5 mL aqua regia (HCl:$HNO_3$ = 3:1, v:v). Certified reference materials (NIST SRM 2711, Montana soil II; MESS-1, estuary sediment) were prepared in every 10 samples. The digest solutions of samples were diluted to 0.5 ng $mL^{-1}$ based on THg values measured by the Nippon MA-2 combustion system. Sample solutions were diluted to have acid concentrations of < 20% (v/v). Hg concentrations and acid matrices in the bracketing NIST SRM 3133 solutions were matched with 10% of the neighbouring samples. THg in sample digests was monitored by MC-ICP-MS using $^{202}Hg$ signals. The THg values estimated by $^{202}Hg$ signals were 94 to 109% to those measured by the Nippon MA-2 combustion system. MDF is expressed in $\delta^{202}Hg$ notation in units of ‰ referenced to the NIST-3133 Hg standard (analyzed before and after each sample):

$$\delta^{202}Hg(‰) = [(^{202}Hg/^{198}Hg_{sample})/(^{202}Hg/^{198}Hg_{standard}) - 1] \times 1000 \quad (1)$$

MIF is reported in Δ notation, which describes the difference between the measured $\delta^{xxx}Hg$ and the theoretically predicted $\delta^{xxx}Hg$ value, in units of ‰:

$$\Delta^{xxx}Hg \approx \delta^{xxx}Hg - \delta^{202}Hg \times \beta \quad (2)$$

β is equal to 0.2520 for $^{199}Hg$, 0.5024 for $^{200}Hg$, and 0.7520 for $^{201}Hg$ (Blum and Bergquist, 2007).

Analytical uncertainty was estimated based on replication of the UM-Almadén secondary standard solution, and full procedural analyses of standard reference materials (MESS-1 and NIST SRM 2711). The overall average and uncertainty of all UM-Almadén measurements ($\delta^{202}Hg$: − 0.50 ± 0.08‰; $\Delta^{199}Hg$: − 0.03 ± 0.05‰; $\Delta^{200}Hg$: 0.02 ± 0.04‰; $\Delta^{201}Hg$: − 0.02 ± 0.04‰; 2SD, $n$ = 9) agreed well with previous results (Blum and Bergquist, 2007). Measurements of replicate digests of NIST 2711 ($\delta^{202}Hg$: − 0.24 ± 0.10‰; $\Delta^{199}Hg$: − 0.19 ± 0.05‰; $\Delta^{200}Hg$: 0.02 ± 0.03‰; $\Delta^{201}Hg$: − 0.19 ± 0.04‰, 2SD, $n$ = 3) and MESS-1 ($\delta^{202}Hg$ − 1.91 ± 0.08‰; $\Delta^{199}Hg$ 0.02 ± 0.04‰; $\Delta^{200}Hg$: 0.03 ± 0.03‰; $\Delta^{201}Hg$: 0.03 ± 0.04‰; 2SD, $n$ = 3) were also comparable with previous studies (Biswas et al., 2008; Lefticariu et al., 2011; Donovan et al., 2013;Yin et al., 2014; Lepak et al., 2015).

## 4. Results

### 4.1. Elemental concentrations

The bulk geochemical and isotope data are listed in Table 1. At Maoshi, the black shales have 2.0 to 4.5 wt% TS, 6.5 to 9.3 wt% TOC, and 0.17 to 3.62 wt% $P_2O_5$, while the two polymetallic sulfide-rich samples have about 20 wt% TS, about 20 wt% TOC, and about 4 wt% $P_2O_5$. The polymetallic sulfide-rich samples have Mo (42,400 to 75,300 μg $g^{-1}$) and Hg (10,900 to 20,700 ng $g^{-1}$) which are

**Table 1**
Sampling information and analytical results.

| Sample | Lithology | Depth[a] | TS | TOC | $P_2O_5$ | Mo | Hg | $\delta^{202}Hg$ | $\Delta^{199}Hg$ | $\Delta^{200}Hg$ | $\Delta^{201}Hg$ |
|---|---|---|---|---|---|---|---|---|---|---|---|
| ID | | m | % | % | % | μg $g^{-1}$ | ng $g^{-1}$ | ‰ | ‰ | ‰ | ‰ |
| Maoshi polymetallic unit | | | | | | | | | | | |
| MSU-10 | Black shale | 1.0 | 4.04 | 7.49 | 0.17 | 88.5 | 326.8 | − 1.71 | 0.10 | 0.07 | 0.12 |
| MSU-8 | Black shale | 0.8 | 2.00 | 6.50 | 0.20 | 81.9 | 219.9 | − 1.74 | 0.12 | 0.04 | 0.1 |
| MSU-6 | Black shale | 0.6 | 2.72 | 7.61 | 0.21 | 155.0 | 278.7 | − 1.89 | 0.18 | 0.05 | 0.13 |
| MSU-4 | Black shale | 0.4 | 4.30 | 8.01 | 0.19 | 129.0 | 396.5 | − 1.93 | 0.16 | 0.07 | 0.13 |
| MSU-2 | Black shale | 0.2 | 2.70 | 8.57 | 0.20 | 341.0 | 178.0 | − 2.12 | 0.16 | 0.10 | 0.13 |
| MS-0 | Ni-Mo Ore | 0.0 | 19.3 | 23.3 | 3.72 | 75,290 | 20,725 | − 3.02 | 0.18 | 0.05 | 0.14 |
| SL-0 | Ni-Mo Ore | 0.0 | 18.5 | 20.5 | 4.11 | 42,420 | 10,886 | − 2.43 | 0.17 | 0.05 | 0.18 |
| MSL-1 | Black shale | − 0.1 | 2.41 | 9.23 | 3.62 | 166.0 | 406.7 | − 2.70 | 0.15 | 0.10 | 0.20 |
| MSL-2 | Black shale | − 0.2 | 4.12 | 8.80 | 0.23 | 119.0 | 480.1 | − 2.97 | 0.14 | 0.06 | 0.13 |
| MSL-3 | Black shale | − 0.3 | 4.51 | 9.32 | 0.22 | 194.0 | 504.8 | − 2.42 | 0.22 | 0.09 | 0.21 |
| Zhijin P deposit | | | | | | | | | | | |
| 2K1101-7 | Black shale | 298.7 | 1.21 | 1.54 | 0.19 | 12 | 46.2 | − 2.17 | 0.11 | 0.05 | 0.11 |
| 2K1101-12 | Black shale | 302.5 | 0.79 | 1.53 | 0.19 | 12.1 | 43.1 | − 2.31 | − 0.01 | − 0.06 | 0.03 |
| 2K1101-18 | Black shale | 306.0 | 0.93 | 1.54 | 0.18 | 13.8 | 31.7 | − 2.46 | 0.08 | − 0.04 | 0.11 |
| 2K1101-23 | Black shale | 309.3 | 0.73 | 1.31 | 0.20 | 7.2 | 30.9 | − 2.18 | 0.09 | − 0.04 | 0.09 |
| 2K1101-28 | Black shale | 312.1 | 0.76 | 1.75 | 0.23 | 17.9 | 38.8 | − 2.37 | 0.09 | 0.02 | 0.12 |
| 2K1101-33 | Black shale | 314.6 | 0.79 | 1.72 | 0.19 | 25.9 | 35.3 | − 2.40 | 0.10 | 0.01 | 0.10 |
| 2K1101-38 | Black shale | 316.8 | 1.41 | 1.88 | 0.16 | 8.8 | 43.9 | − 2.78 | 0.13 | 0.03 | 0.13 |
| 2K1101-43 | Black shale | 319.5 | 1.68 | 2.19 | 0.13 | 8.3 | 66.8 | − 2.41 | 0.12 | 0.07 | 0.15 |
| 2K1101-48 | Black shale | 322.0 | 2.07 | 2.60 | 0.22 | 10.3 | 93.4 | − 2.00 | 0.05 | − 0.02 | 0.10 |
| 2K1101-53 | Black shale | 324.3 | 1.92 | 2.52 | 0.23 | 9.0 | 78.4 | − 1.84 | 0.08 | 0.08 | 0.11 |
| 2K1101-59 | Black shale | 327.9 | 2.10 | 2.58 | 0.23 | 8.4 | 84.3 | − 1.86 | 0.09 | 0.07 | 0.15 |
| 2K1101-63 | Black shale | 329.9 | 1.87 | 2.41 | 0.22 | 9.1 | 108.6 | − 1.72 | 0.22 | 0.07 | 0.21 |
| 2K1101-69 | Black shale | 332.9 | 2.72 | 2.95 | 0.23 | 16.6 | 289.6 | − 1.18 | 0.05 | 0.06 | 0.09 |
| 2K1101-74 | Black shale | 335.0 | 4.33 | 5.24 | 0.15 | 54.0 | 529.4 | − 1.25 | 0.13 | 0.06 | 0.19 |
| 2K1101-80 | Black shale | 337.4 | 1.37 | 1.03 | 5.14 | 10.0 | 183.9 | − 1.13 | 0.11 | 0.04 | 0.16 |
| 2K1101-89 | Phosphorite | 342.4 | 0.60 | 0.48 | 9.83 | 0.6 | 91.9 | − 0.95 | 0.13 | 0.06 | 0.13 |
| 2K1101-99 | Phosphorite | 348.0 | 0.75 | 0.98 | 11.08 | 1.5 | 180.3 | − 1.38 | 0.13 | 0.06 | 0.08 |
| 2K1101-105 | Phosphorite | 350.5 | 1.84 | 1.50 | 29.37 | 8.6 | 1536 | − 1.61 | 0.24 | 0.10 | 0.22 |
| 2K1101-111 | Phosphorite | 354.7 | 3.24 | 2.68 | 27.45 | 9.1 | 2171 | − 1.46 | 0.20 | 0.10 | 0.20 |
| 2K1101-117 | Phosphorite | 359.5 | 0.59 | 0.86 | 22.34 | 8.3 | 1179 | − 1.58 | 0.18 | 0.05 | 0.17 |

[a] For Zhijin samples, the sample depth indicates distance from surface in the drill core; For Maoshi samples, the Ni-Mo ore layer is defined as 0 m, locations of other samples are relative to the Ni-Mo ore layer.

significantly higher than in the black shales above and below (Mo: 88.5 to 341 μg $g^{-1}$; Hg: 178 to 505 ng $g^{-1}$). TS/TOC ratios for the polymetallic Ni-Mo-sulfide samples (0.83 to 0.90) are slightly higher than those of the black shales (0.26 to 0.54) (Fig. 3).

Compared to the Maoshi black shale, black shales at Zhijin have similar $P_2O_5$ concentration (0.13 to 5.14 wt%), relatively lower TS (0.80 to 4.30 wt%), TOC (1.00 to 5.20 wt%), Mo (7.2 to 54.0 μg $g^{-1}$) and Hg (31.7 to 529 ng $g^{-1}$), but relatively higher TS/TOC ratios (0.43 to 1.33) (Fig. 3). Within the Zhijin deposit, phosphorite samples have relatively lower TS (0.6 to 3.2 wt%), TOC (0.5 to 2.7 wt%) and Mo (0.6 to 9.1 μg $g^{-1}$) concentrations than in the black shales. However, the phosphorite samples have higher $P_2O_5$ (9.8 to 27.5 wt%), Hg (91.9 to 2170 ng $g^{-1}$) and TS/TOC ratios (0.69 to 1.25).

### 4.2. Mercury isotope compositions

The distribution of Hg isotopic compositions is also shown in Fig. 3. Black shales at Maoshi have $\delta^{202}Hg$ values of − 2.70 to − 1.71‰ and $\Delta^{199}Hg$ values of 0.10 to 0.22‰. The polymetallic sulfide ores show more negative $\delta^{202}Hg$ (− 3.02 to − 2.43‰) but similar $\Delta^{199}Hg$ (0.17 to 0.18‰) than the host black shales. Black shales at Maoshi have $\delta^{202}Hg$ values of − 2.97 to − 1.13‰ and $\Delta^{199}Hg$ values of − 0.01 to 0.22‰. Compared to the host black shales, the phosphorite has less negative $\delta^{202}Hg$ values (− 1.61 to − 0.95‰). Positive $\Delta^{199}Hg$ values ($\Delta^{199}Hg$: 0.13 to 0.24‰) were also observed for the phosphorite. The average $\Delta^{199}Hg/\Delta^{201}Hg$ of all our samples is 1.22 ± 0.14 (Fig. 4), similar to previously reported values for aqueous Hg(II) photo-reduction driven by natural dissolved OM ($\Delta^{199}Hg/\Delta^{201}Hg$: 1.02 ± 0.02) (Bergquist and Blum, 2007). Small but significant $\Delta^{200}Hg$ values in the Maoshi and Zhijin samples range from 0.04 to 0.10‰ and − 0.06 to 0.10‰, respectively (Fig. 3).

## 5. Discussion

### 5.1. Marine redox conditions revealed by TOC and TS

The global C and S cycles are intimately linked by biotic and abiotic processes, which are influenced by marine redox conditions (Berner, 1984). The amount of OM is an important control on the amount of TS that can form in marine sediments and typically results in a generally positive correlation between sediment TOC and TS (Fig. 5) (Berner, 1984). High TS sediments are linked to bacterial sulfate reduction under locally suboxic to euxinic conditions, while low TS in marine sediments with lower sedimentation rates and without significant input of freshwater hint at higher oxidation state which may cause oxic biodegradation of OM (Walker, 1986). All polymetallic sulfide-rich and phosphorite samples show a TS/TOC of ~0.86, much higher than normal marine sediments (TS/TOC ~ 0.3) and our other black shales (~0.46). This is in agreement with rapid burial of OM and extensive bacterial sulfate reduction during sedimentation. Previous studies suggested that the phosphorite samples formed under suboxic conditions (Papineau, 2010), whereas the polymetallic sulfide-rich samples formed under euxinic conditions with restricted sulfate supply (Murowchick et al., 1994; Lehmann et al., 2007).

### 5.2. Phosphorus and Mo concentrations controlled by marine conditions

$P_2O_5$ concentrations are the highest in phosphorites, followed by the polymetallic Ni-Mo-sulfide and black shale samples of each site (Fig. 3). There are no clear correlations between $P_2O_5$ and TS, and TOC.

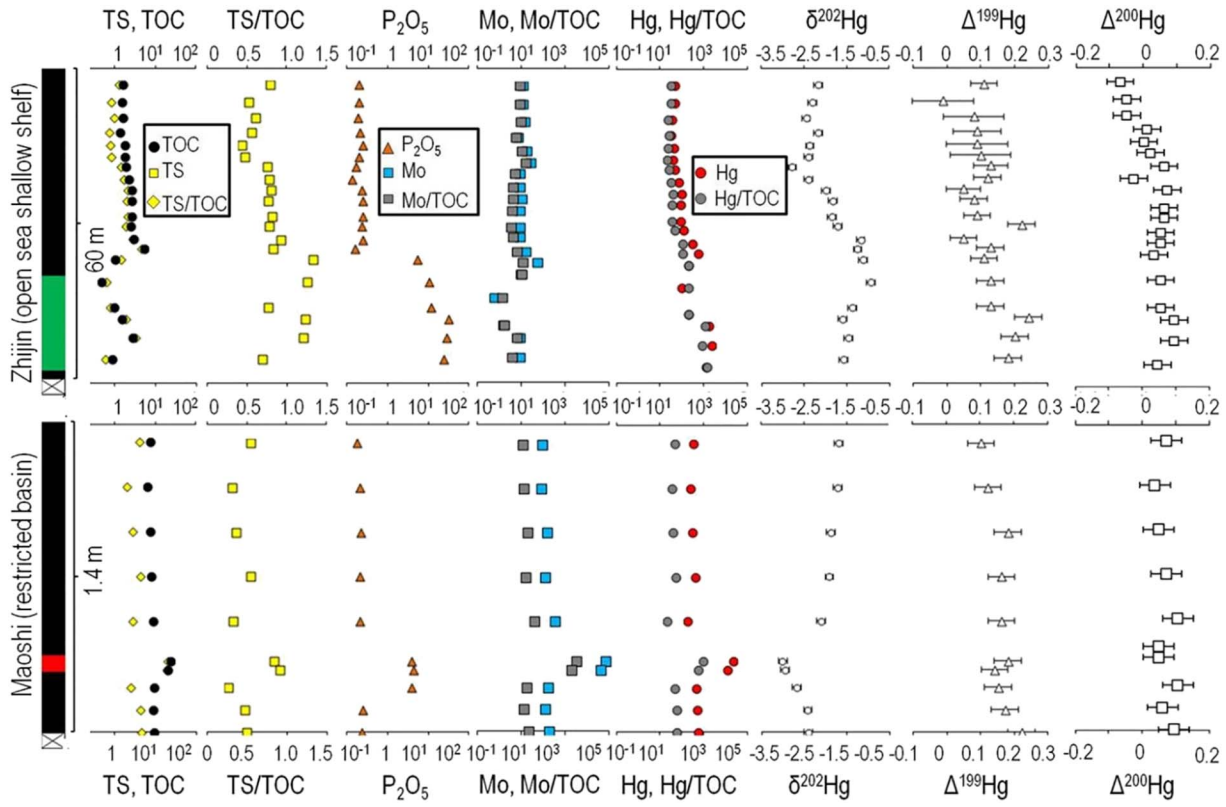


**Fig. 3.** Stratigraphic distribution of TS, TOC, TS/TOC, $P_2O_5$, Mo and Hg concentrations, Mo/TOC and Hg/TOC ratios, and $\delta^{202}Hg$, $\Delta^{199}Hg$ and $\Delta^{200}Hg$ for the Maoshi and Zhijin samples. Error bars are 2SD. Green column represents the phosphorite layer, and red column represents the polymetallic sulfide-rich black shale. (For interpretation of the references to colour in this figure legend, the reader is referred to the web version of this article.)

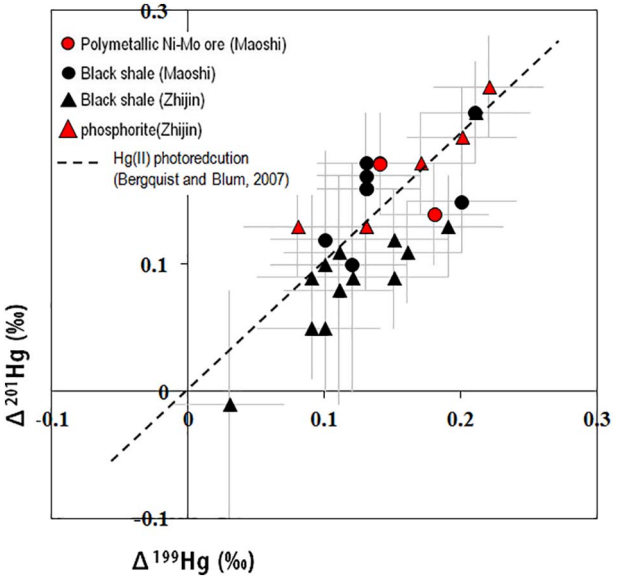


**Fig. 4.** Relationship between $\Delta^{201}Hg$ and $\Delta^{199}Hg$ for the Maoshi and Zhijin samples. Gray bars are analytical error (2SD).

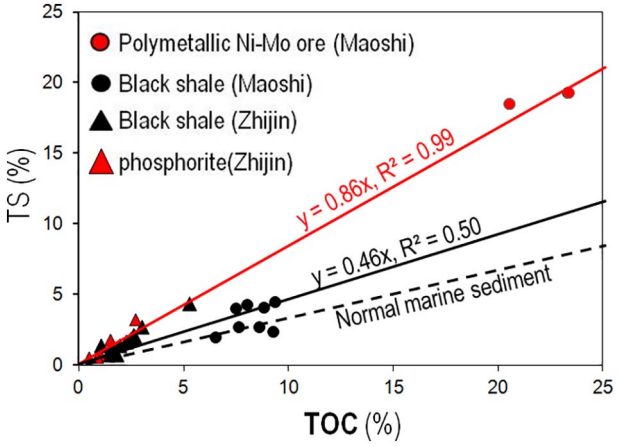


**Fig. 5.** Relation between TOC and TS for the Maoshi and Zhijin samples. The polymetallic sulfide-rich and phosphorite samples define the red solid correlation line; the black shales define black solid line; and the black dashed line represents normal marine sediments (TS/TOC: ~0.3, Berner, 1984). (For interpretation of the references to colour in this figure legend, the reader is referred to the web version of this article.)

Upwelling of nutrient-rich seawater at the Yangtze continental margin during the Early Cambrian has been suggested as the main cause of both polymetallic mineralization and phosphorite formation (Lehmann et al., 2007). The enhanced availability of nutrients would have resulted in increased bioproductivity in the photic zone. Deposition and decomposition of OM would have caused dysoxic and anoxic conditions in the deeper water column and at the seafloor. The highest $P_2O_5$ concentrations in phosphorite samples (9.8 to 27.5 wt%) agree well with the fact that phosphogenesis is typical of shallow shelf settings under suboxic conditions (Papineau, 2010), whereas the relatively lower but still elevated $P_2O_5$ concentrations in the polymetallic Ni-Mo-sulfide samples (4 wt% $P_2O_5$) relate to a detrital apatite component in these sediments which was washed in from the nearby suboxic environment (Kříbek et al., 2007; Lehmann et al., 2016).

Molybdenum contents in both deposits are positively correlated with TS and TOC (Fig. 6). Anoxic conditions are favorable for OM sedimentation, and OM is rich in reduced sulfur (-S) and thiol (-SH) groups (Grasby et al., 2013). The concentrations of Mo in the seawater column of anoxic basins are usually lower than in oxic seawater because

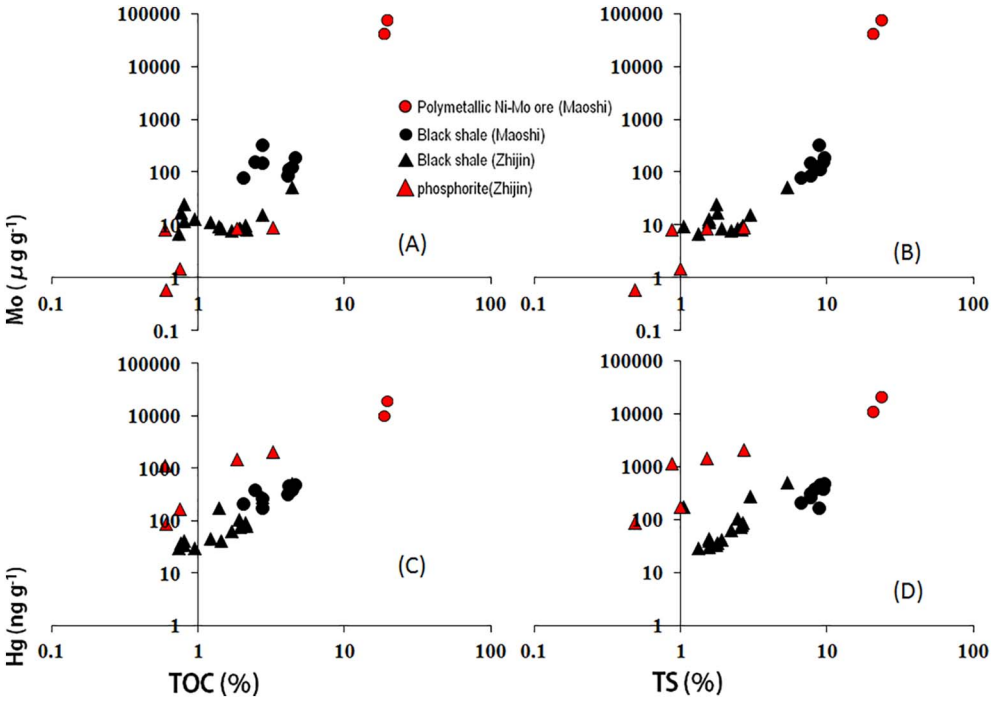


**Fig. 6.** Relationship between Mo-Hg concentrations and TOC, and TS for the Maoshi and Zhijin samples.

of preferential uptake into anoxic and sulfidic sediments (Emerson and Huested, 1991). Mo is normalized to TOC to account for the drawdown by OM (Fig. 3). Compared to the black shale samples of each site, exceptionally high Mo/TOC ratios of 2070 to 3230 (μg $g^{-1}$/wt%) are observed in the Maoshi polymetallic sulfide-rich unit. Phosphorite samples at Zhijin have much lower Mo/TOC ratios of 1.3 to 9.7. The higher Mo content and Mo/TOC ratios of the polymetallic Ni-Mo-sulfide samples reflect effective precipitation (sulfide control) of Mo in a restricted euxinic basin with a high degree of decay of OM either in the water column or at the seafloor (Lehmann et al., 2007). In comparison, lower Mo concentrations and Mo/TOC ratios of the phosphorite suggest less effective precipitation of Mo in an open shallow shelf under suboxic conditions.

### 5.3. Mercury isotopes indicate a seawater source of Hg

Mercury concentration at both sites is positively correlated with TS and TOC content (Fig. 6), consistent with the fact that Hg can be effectively scavenged by OM. Unlike Mo, anomalously high Hg/TOC ratios (531 to 889; ng $g^{-1}$/wt%), were not only observed in the polymetallic sulfide-rich samples from Maoshi, but also in the Zhijin phosphorite (184 to 1370). The high Hg/TOC may be explained by enhanced adsorption of Hg by organic particles under dysoxic and anoxic conditions. Mercury isotopes may provide insight into the origin of this Hg anomaly. As shown in Fig. 7, our Early Cambrian black shale samples reveal some of the most negative $\delta^{202}$Hg values compared to other organic-rich marine deposits, e.g., mid-Pleistocene Mediterranean sapropels (Gehrke et al., 2009), end-Permian black shales from the Sverdrup Basin, Canada (Grasby et al., 2017), Eocene black shales from the Arctic Basin (Gleason et al., 2017), and end-Triassic shelf sediments (Thibodeau et al., 2016). However, the $\Delta^{199}$Hg values are within the range of previous results. The variations of $\delta^{202}$Hg can result from various geochemical processes that cause MDF. However, the MIF signature of Hg is likely more useful to indicate the Hg source; this is because Hg-MIF in natural samples mainly occurs during photochemical processes (see Sonke, 2011; Blum et al., 2014, for summaries) and post-depositional processes seem unlikely to alter the MIF signature (Thibodeau et al., 2016; Gleason et al., 2017; Grasby et al., 2017).

Mercury mainly enters the ocean either though atmospheric deposition or runoff from the terrestrial environment via rivers (Yin et al., 2015). Scavenging of oxidized Hg species by precipitation is an important pathway for depositing atmospheric Hg (Gratz et al., 2010). MIF of odd Hg isotopes is believed to be conservative due to the relatively low photochemical processing which particulate-associated Hg undergoes (Lepak et al., 2015). Terrestrial soils have been shown to have negative $\Delta^{199}$Hg values (− 0.25 to 0.00‰) (Biswas et al., 2008). Modern seawater mainly has positive $\Delta^{199}$Hg of 0.1 to 0.4‰, similar to precipitation-derived Hg (0.0 to 1.0‰) (Gratz et al., 2010; Chen et al., 2012; Štrok et al., 2015). Positive $\Delta^{199}$Hg in precipitation and seawater is explainable by photoreduction of Hg(II) species in cloud droplets and in the surface ocean. In our study (Fig. 7), positive $\Delta^{199}$Hg values (0.1 to 0.3‰) for black shale samples from Zhijin and Maoshi are quite different from the Eocene black shales from the Arctic Basin (Gleason et al., 2017) and the end-Triassic shelf sediments in Canada (Thibodeau et al., 2016), which mainly showed less positive to negative $\Delta^{199}$Hg values; these values have been explained by the contribution of continental or volcanic Hg sources. Positive $\Delta^{199}$Hg values were also reported in mid-Pleistocene Mediterranean sapropels (Gehrke et al., 2009) and end-Permian black shales from the Sverdrup Basin, Canada (Grasby et al., 2017), and this has been explained by scavenging of seawater Hg by organic matter. In our study, the observation of positive $\Delta^{199}$Hg values for the black shale samples suggests that Hg is mainly seawater-derived.

Polymetallic sulfide-rich black shale and the phosphorite show positive $\Delta^{199}$Hg values similar to the black shales, suggesting Hg in these rock units also originated from seawater. Previous studies have suggested that the polymetallic sulfide-rich black shale and the phosphorites are of submarine-hydrothermal exhalative origin (Jiang et al., 2007). However, our data do not support this hypothesis because hydrothermal fluids from the sea floor have been shown to have $\Delta^{199}$Hg ~ 0 (Sherman et al., 2009). Metal scavenging from seawater by OM can better explain these results. The origin of Hg from seawater is also supported by MIF of $^{200}$Hg. Some of our samples show $\Delta^{200}$Hg of up to 0.10‰ (Fig. 8), and the MIF signal is significant when compared to the analytical uncertainty ( ± 0.04‰, 2SD). MIF of $^{200}$Hg has been observed in modern seawater (Štrok et al., 2015). In sediments, $\Delta^{200}$Hg provides evidence of a significant atmospheric component (Lepak et al., 2015), because processes inducing $\Delta^{200}$Hg anomalies likely occur in the

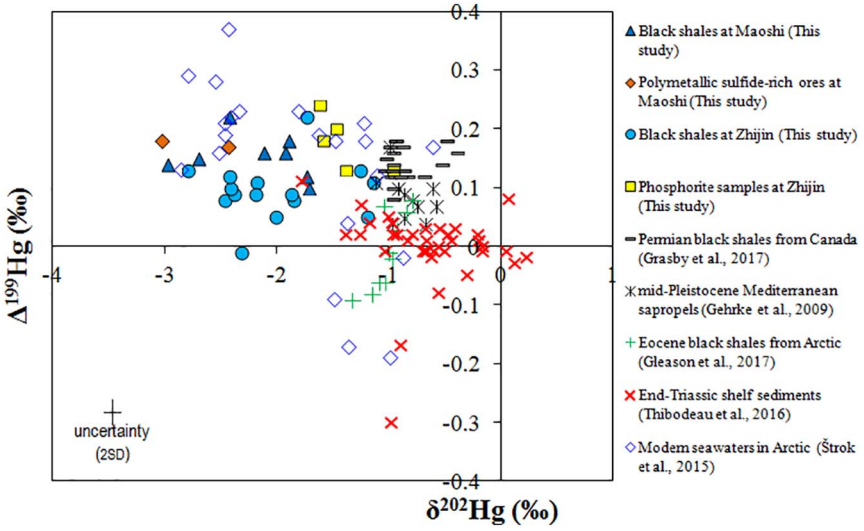


**Fig. 7.** $\delta^{202}$Hg vs. $\Delta^{199}$Hg for the Early Cambrian black shales compared with mid-Pleistocene Mediterranean sapropels (Gehrke et al., 2009), the end-Permian black shales from the Sverdrup Basin, Canada (Grasby et al., 2017), Eocene black shales from the Arctic Basin (Gleason et al., 2017), the end Triassic shelf sediments (Thibodeau et al., 2016) and modern Arctic seawaters (Štrok et al., 2015).

atmosphere and are carried to the oceans by precipitation (Chen et al., 2012).

Under certain circumstances, the variation of $\delta^{202}$Hg can reflect source changes if Hg is transported by particles (Foucher and Hintelmann, 2009; Sial et al., 2016). Runoff of soils is relatively conservative because Hg is mostly carried in the particulate phase. However, atmospheric deposition contains a substantial amount of soluble Hg species, which may be isotopically altered during deposition and diagenesis. The MDF signature may be altered during various geochemical processes (Blum et al., 2014). Compared to the black shales of each site, the polymetallic sulfide-rich samples at Maoshi have slightly lower $\delta^{202}$Hg, and the Zhijin phosphorite samples have higher $\delta^{202}$Hg (Fig. 3). Given the fact that Hg is mainly derived from seawater as supported by MIF of $^{199}$Hg and $^{200}$Hg, this likely reflects changes of seawater $\delta^{202}$Hg composition. Štrok et al. (2015) reported lower $\delta^{202}$Hg in deep seawater compared to surface water in the North Arctic ocean, while the seawater $\Delta^{199}$Hg values were relatively constant at different depth. The more negative $\delta^{202}$Hg for the polymetallic sulfide-rich samples may reflect their deeper basin setting. However, this explanation is not consistent with the relatively negative $\delta^{202}$Hg for black shales at Maoshi (restricted basin) compared to Zhijin (open-sea shallow shelf). The more negative $\delta^{202}$Hg for the polymetallic sulfide-rich samples compared to the phosphorites is explainable by the formation of Hg sulfide (HgS) under euxinic conditions, together with Ni, Mo and other metal sulfides. Formation of HgS has been shown to result in a negative shift of $-0.6$‰ in $\delta^{202}$Hg of the solid phase (Foucher et al., 2013), similar to the offset in $\delta^{202}$Hg between the polymetallic sulfide-rich samples and the normal black shales at Maoshi. Precipitation of HgS may also cause higher $\delta^{202}$Hg of Hg(II) in seawater above the anoxic water column, as supported by the higher $\delta^{202}$Hg in the Zhijin phosphorite samples.

## 6. Conclusions

Mercury isotopes suggest seawater is an important source of Hg in our samples. Seawater Hg may also have mixed with other sources (e.g., venting hydrothermal fluids), resulting in less positive $\Delta^{199}$Hg and $\Delta^{200}$Hg values compared to the modern ocean (Figs. 7 and 8), such mixing cannot completely ruled out due to the lack of Hg isotope data on Early Cambrian seawater, but the hydrothermal component must be very minor compared to the positive seawater signal. The conceptual model in Fig. 9 summarizes our interpretation. The phosphorites and polymetallic sulfide-rich black shale formed stratigraphically equivalent in a continental-margin setting (i.e., shallow open shelf and deeper

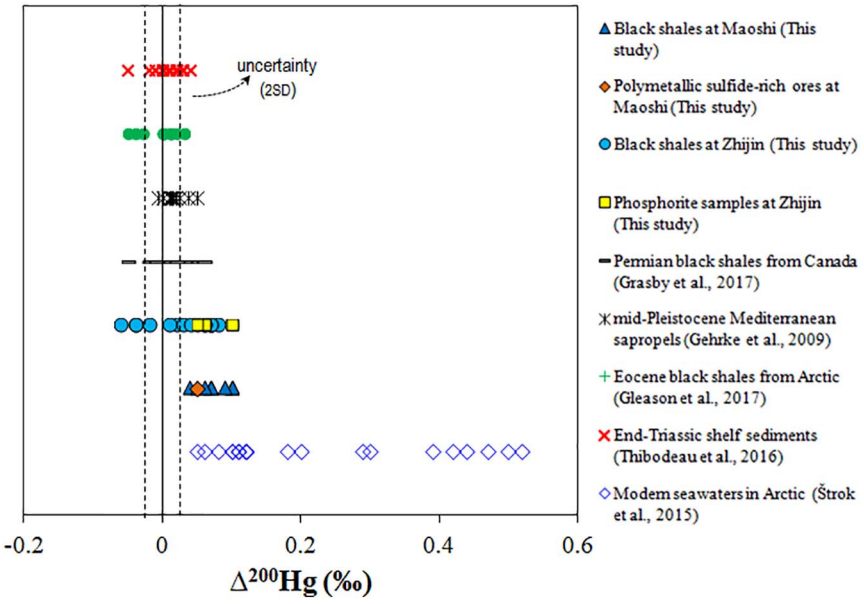


**Fig. 8.** Magnitudes of $\Delta^{200}$Hg for the Early Cambrian black shales compared with mid-Pleistocene Mediterranean sapropels (Gehrke et al., 2009), end Permian black shales from the Sverdrup Basin, Canada (Grasby et al., 2017), Eocene black shales from the Arctic Basin (Gleason et al., 2017), the end-Triassic shelf sediments (Thibodeau et al., 2016) and modern Arctic seawaters (Štrok et al., 2015).

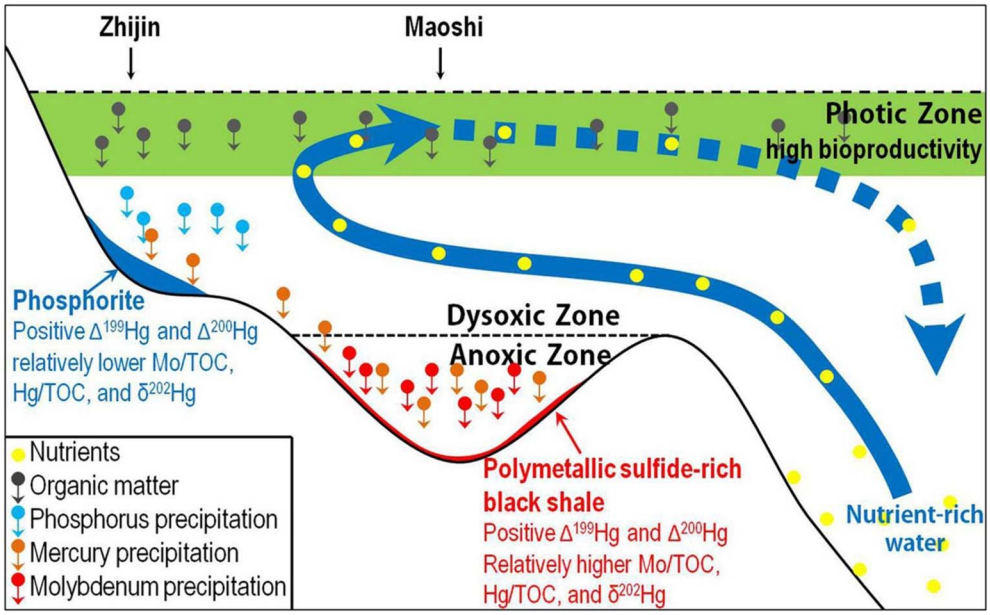


**Fig. 9.** Schematic diagram illustrating conceptual geochemical cycling of P, Mo and Hg for the Early Cambrian continental margin of the Yangtze Platform in South China.

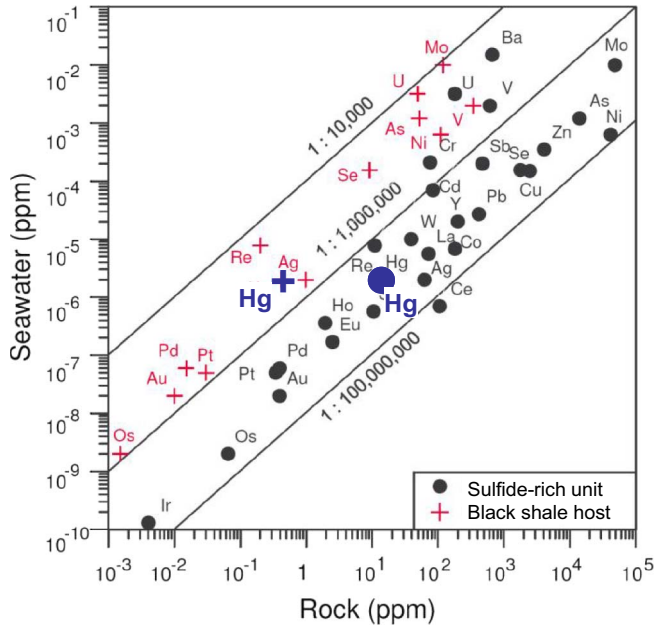


**Fig. 10.** Mercury content in the polymetallic sulfide-rich black shale unit and the over- and underlying normal black shale, compared to other redox- and bio-sensitive metals (Lehmann et al., 2007). Note the enrichment of many elements compared to average modern seawater of about $10^7$.

restricted basin, respectively) with upwelling of nutrient-rich open ocean waters. Extensive bioproductivity in the photic zone produced large quantities of OM that scavenged phosphorus and metals (e.g., Hg). Deposition and decomposition of OM caused dysoxic and anoxic/sulfidic conditions in the deeper water column and at the seafloor. Decomposition of OM also released phosphorus to the water column, which was fixed in the suboxic shallow shelf setting. The deeper basin was less favorable for phosphogenesis because phosphorus is much more soluble under anoxic conditions. Sulfur-containing ligands (e.g., -S, -SH) from OM and from bacterial sulfate reduction immobilized many redox-sensitive metals, including Hg. The positive $\Delta^{199}$Hg and $\Delta^{200}$Hg values of our samples provide direct evidence that Hg originated from seawater. The distinct variation in $\delta^{202}$Hg is likely caused by precipitation of HgS in euxinic parts of the basin, which reflects extensive burial and remineralization of OM.

The enrichment in Hg is only part of spectacular enrichment of a broad redox- and bio-sensitive metal spectrum (Lehmann et al., 2007). This enrichment was possible in a favorable paleoenvironmental setting along the Early Cambrian continental margin of the drowned Yangtze Platform, which gave rise to great biodiversity and a large spectrum of sedimentary rocks. Locally restricted basins with euxinic bottom water along the rifted shelf acted as traps of metals released from decaying biomass, and remineralization at very low clastic sedimentation rate allowed enrichment of Hg and other redox- and bio-sensitive metals on the order of $10^7$ compared to modern seawater (Fig. 10). Such enrichment is otherwise only known in a completely different marine environment, the oxic deep-sea of the modern oceans with their manganese nodules and crusts (Hein and Koschinsky, 2014).

## Acknowledgements

Runsheng Yin was funded by the Chinese Academy of Sciences through the Hundred Talent Plan. This work was supported by the Natural Science Foundation of China (41303014, 41403008), the National Nonprofit Institute Research Grant (YWF201406), and the National Basic Research Program of China (No: 2014CB953701). We thank USGS Wisconsin Mercury Research Lab for providing instrument time for Hg concentration and isotopic composition analysis.

## References

Bédard, L.P., Savard, D., Barnes, S.J., 2008. Total sulfur concentration in geological reference materials by elemental infrared analyser. Geostand. Geoanal. Res. 32, 203–208.

Bergquist, B.A., Blum, J.D., 2007. Mass-dependent and -independent fractionation of Hg isotopes by photoreduction in aquatic systems. Science 318, 417–420.

Bergquist, B.A., Blum, J.D., 2009. The odds and evens of mercury isotopes: applications of mass-dependent and mass-independent isotope fractionation. Elements 5, 353–357.

Berner, R.A., 1984. Sedimentary pyrite formation: an update. Geochim. Cosmochim. Acta 48, 605–615.

Biswas, A., Blum, J.D., Keeler, G.J., 2008. Mercury storage in surface soils in a central Washington forest and estimated release during the 2001 Rex Creek Fire. Sci. Total Environ. 404, 129–138.

Blum, J.D., Bergquist, B.A., 2007. Reporting of variations in the natural isotopic composition of mercury. Anal. Bioanal. Chem. 388 (2), 353–359.

Blum, J.D., Sherman, L.S., Johnson, M.W., 2014. Mercury isotopes in earth and environmental sciences. Annu. Rev. Earth Planet. Sci. 42, 249–269.

Chen, J., Hintelmann, H., Feng, X., Dimock, B., 2012. Unusual fractionation of both odd and even mercury isotopes in precipitation from Peterborough, ON, Canada. Geochim. Cosmochim. Acta 90, 33–46.

Donovan, P.M., Blum, J.D., Yee, D., Gehrke, G.E., Singer, M.B., 2013. An isotopic record of mercury in San Francisco Bay sediment. Chem. Geol. 349, 87–98.
Emerson, S.R., Huested, S.S., 1991. Ocean anoxia and the concentrations of molybdenum and vanadium in seawater. Mar. Chem. 34, 177–196.
Foucher, D., Hintelmann, H., 2009. Tracing mercury contamination from the Idrija Mining Region (Slovenia) to the Gulf of Trieste using Hg isotope ratio measurements. Environ. Sci. Technol. 43, 33–39.
Foucher, D., Hintelmann, H., Al, T.A., MacQuarrie, K.T., 2013. Mercury isotope fractionation in waters and sediments of the Murray Brook mine watershed (New Brunswick, Canada): tracing mercury contamination and transformation. Chem. Geol. 336, 87–95.
Gehrke, G.E., Blum, J.D., Meyers, P.A., 2009. The geochemical behavior and isotopic composition of Hg in a mid-Pleistocene western Mediterranean sapropel. Geochim. Cosmochim. Acta 73, 1651–1665.
Gleason, J.D., Blum, J.D., Moore, T.C., Polyak, L., Jakobsson, M., Meyers, P.A., Biswas, A., 2017. Sources and cycling of mercury in the paleo Arctic Ocean from Hg stable isotope variations in Eocene and quaternary sediments. Geochim. Cosmochim. Acta 197, 245–262.
Grasby, S.E., Sanei, H., Beauchamp, B., Chen, Z., 2013. Mercury deposition through the Permo-Triassic biotic crisis. Chem. Geol. 351, 209–216.
Grasby, S.E., Shen, W., Yin, R., Gleason, J.D., Blum, J.D., Lepak, R.F., Hurley, J.P., Beauchamp, B., 2017. Isotopic signatures of mercury contamination in latest Permian oceans. Geology 45, 55–58.
Gratz, L.E., Keeler, G.J., Blum, J.D., Sherman, L.S., 2010. Isotopic composition and fractionation of mercury in Great Lakes precipitation and ambient air. Environ. Sci. Technol. 44, 7764–7770.
Hein, J.R., Koschinsky, A., 2014. Deep-ocean ferromanganese crusts and nodules. In: Scott, S. (Ed.), Treatise on Geochemistry. vol. 12. Elsevier, New York, pp. 273–291.
Jiang, S.Y., Chen, Y.Q., Ling, H.F., Yang, J.H., Feng, H.Z., Ni, P., 2006. Trace- and rare-earth element geochemistry and Pb-Pb dating of black shales and intercalated Ni-Mo-PGE-Au sulfide ores in Lower Cambrian strata, Yangtze platform, South China. Mineral. Deposita 41, 453–467.
Jiang, S., Yang, J., Ling, H., Chen, Y., Feng, H., Zhao, K., Ni, P., 2007. Extreme enrichment of polymetallic Ni-Mo-PGE-Au in Lower Cambrian black shales of South China: an Os isotope and PGE geochemical investigation. Palaeogeogr. Palaeoclimatol. Palaeoecol. 254, 217–228.
Kao, L.S., Peacor, D.R., Coveney, R.M., Zhao, G.M., Dungey, K.E., Curtis, D., Penner-Hahn, J.E., 2001. A C/MoS2 mixed-layer phase (MoSC) occurring in metalliferous black shales from southern China, and new data on jordisite. Can. Mineral. 86, 852–861.
Kimura, H., Watanabe, Y., 2001. Oceanic anoxia at the Precambrian-Cambrian boundary. Geology 29, 995–998.
Kříbek, B., Sýkorová, I., Pašava, J., Machovič, V., 2007. Organic geochemistry and petrography of barren and Mo–Ni–PGE mineralized marine black shales of the Lower Cambrian Niutitang Formation (South China). Int. J. Coal Geol. 72, 240–256.
Lefticariu, L., Blum, J.D., Gleason, J.D., 2011. Mercury isotopic evidence for multiple mercury sources in coal from the Illinois Basin. Environ. Sci. Technol. 45, 1724–1729.
Lehmann, B., Nägler, T.F., Holland, H.D., Wille, M., Mao, J., Pan, J., Ma, D., Dulski, P., 2007. Highly metalliferous carbonaceous shale and Early Cambrian seawater. Geology 35, 403–406.
Lehmann, B., Frei, R., Xu, L., Mao, J., 2016. Early Cambrian black shale-hosted Mo-Ni and V mineralization on the rifted margin of the Yangtze platform, China: reconnaissance chromium isotope data and a refined metallogenic model. Econ. Geol. 111, 89–103.
Lepak, R.F., Yin, R., Krabbenhoft, D.P., Ogorek, J.M., DeWild, J.F., Holsen, T.M., Hurley, J.P., 2015. Use of stable isotope signatures to determine mercury sources in the Great Lakes. Environ. Sci. Technol. Lett. 2, 335–341.
Mao, J.W., Lehmann, B., Du, A.D., Zhang, G.D., Ma, D.S., Wang, Y.T., Zeng, M.G., Kerrich, R., 2002. Re-Os dating of polymetallic Ni-Mo-PGE-Au mineralization in lower Cambrian black shales of south China and its geologic significance. Econ. Geol. 97, 1051–1061.
Murowchick, J.B., Coveney Jr., R.M., Grauch, R.I., Eldridge, C.S., Shelton, K.L., 1994. Cyclic variations of sulfur isotopes in Cambrian stratabound Ni-Mo-(PGE-Au) ores of southern China. Geochim. Cosmochim. Acta 58, 1813–1823.
Olund, S.D., 2004. Methods for the preparation and analysis of solids and suspended solids for total mercury. In: U.S. Geological Survey Techniques of Water-Resources Investigations. Book 5, Chapter A8 (accessed March 16, 2007).
Papineau, D., 2010. Global biogeochemical changes at both ends of the Proterozoic: insights from phosphorites. Astrobiology 10, 165–181.
Pašava, J., Frimmel, H., Taiyi, L., Koubová, M., Martínek, K., 2010. Extreme PGE concentrations in Lower Cambrian acid tuff layer from the Kunyang phosphate deposit, Yunnan province, South China—possible PGE source for Lower Cambrian Mo-Ni–polyelement ore beds. Econ. Geol. 105, 1047–1056.
Sanei, H., Grasby, S.E., Beauchamp, B., 2012. Latest Permian mercury anomalies. Geology 40, 63–66.
Schumacher, B.A., 2002. Methods for the Determination of Total Organic Carbon (TOC) in Soils and Sediments. Ecological Risk Assessment Support Center, 2002pp. 1–23.
Sherman, L.S., Blum, J.D., Nordstrom, D.K., McCleskey, R.B., Barkay, T., Vetriani, C., 2009. Mercury isotopic composition of hydrothermal systems in the Yellowstone Plateau volcanic field and Guaymas Basin sea-floor rift. Earth Planet. Sci. Lett. 279, 86–96.
Sial, A.N., Lacerda, L.D., Ferreira, V.P., Frei, R., Marquillas, R.A., Barbosa, J.A., Gaucher, C., Windmöller, C.C., Pereira, N.S., 2013. Mercury as a proxy for volcanic activity during extreme environmental turnover: the Cretaceous-Paleogene transition. Palaeogeogr. Palaeoclimatol. Palaeoecol. 387, 153–164.
Sial, A.N., Chen, J., Lacerda, L.D., Frei, R., Tewari, V.C., Pandit, M.K., Gaucher, C., Ferreira, V.P., Cirilli, S., Peralta, S., Korte, C., Barbosa, J.A., Pereira, N.S., 2016. Mercury enrichment and mercury isotopes in Cretaceous-Paleogene boundary successions: links to volcanism and palaeoenvironmental impacts. Cretac. Res. 66, 60–81.
Sonke, J.E., 2011. A global model of mass independent mercury stable isotope fractionation. Geochim. Cosmochim. Acta 75, 4577–4590.
Steiner, M., Wallis, E., Erdtmann, B.D., Zhao, Y., Yang, R., 2001. Submarine-hydrothermal exhalative ore layers in black shales from South China and associated fossils: insights into a Lower Cambrian facies and bio-evolution. Palaeogeogr. Palaeoclimatol. Palaeoecol. 169, 165–191.
Štrok, M., Baya, P.A., Hintelmann, H., 2015. The mercury isotope composition of Arctic coastal seawater. Compt. Rendus Geosci. 347, 368–376.
Sun, G., Sommar, J., Feng, X., Lin, C.J., Ge, M., Wang, W., Yin, R., Fu, X., Shang, L., 2016. Mass-dependent and-independent fractionation of mercury isotope during gas-phase oxidation of elemental mercury vapor by atomic Cl and Br. Environ. Sci. Technol. 50, 9232–9241.
Taylor, S.R., McLennan, S.M., 1995. The geochemical evolution of the continental crust. Rev. Geophys. 33, 241–265.
Thibodeau, A.M., Ritterbush, K., Yager, J.A., West, A.J., Ibarra, Y., Bottjer, D.J., Berelson, W.M., Bergquist, B.A., Corsetti, F.A., 2016. Mercury anomalies and the timing of biotic recovery following the end-Triassic mass extinction. Nat. Commun. 7, 11147.
Walker, J.C., 1986. Global geochemical cycles of carbon, sulfur and oxygen. Mar. Geol. 70, 159–174.
Wallis, E., 2007. The Climatic and Environmental History of the South Chinese Yangtze Platform During the Neoproterozoic and Early Cambrian: Hydrothermally Active and Salinity Stratified Epicontinental Basins a Key for Understanding the “Cambrian Explosion”? (Ph.D. thesis) TU Berlinpp. 1–227 (in German with English abstract).
Wang, J., Chen, D., Yan, D., Wei, H., Xiang, L., 2012a. Evolution from an anoxic to oxic deep ocean during the Ediacaran-Cambrian transition and implications for bioradiation. Chem. Geol. 306-307, 129–138.
Wang, X., Shi, X., Jiang, G., Zhang, W., 2012b. New U-Pb age from the basal Niutitang formation in South China: implications for dischronous development and condensation of stratigraphic units across the Yangtze platform at the Ediacaran-Cambrian transition. J. Asian Earth Sci. 48, 1–8.
Xu, L., Lehmann, B., Jingwen, M., Wenjun, Q., Andao, D., 2011. Re-Os age of polymetallic Ni-Mo-PGE-Au mineralization in Early Cambrian black shales of South China—a reassessment. Econ. Geol. 106, 511–522.
Xu, L., Lehmann, B., Mao, J., 2013. Seawater contribution to polymetallic Ni-Mo-PGE-Au mineralization in Early Cambrian black shales of South China: evidence from Mo isotope, PGE, trace element, and REE geochemistry. Ore Geol. Rev. 52, 66–84.
Yin, R., Feng, X., Chen, J., 2014. Mercury stable isotopic compositions in coals from major coal producing fields in China and their geochemical and environmental implications. Environ. Sci. Technol. 48, 5565–5574.
Yin, R., Feng, X., Chen, B., Zhang, J., Wang, W., Li, X., 2015. Identifying the sources and processes of mercury in subtropical estuarine and ocean sediments using Hg isotopic composition. Environ. Sci. Technol. 49, 1347–1355.
Yin, R., Feng, X., Hurley, J.P., Krabbenhoft, D.P., Lepak, R.F., Kang, S., Yang, H., Li, X., 2016. Historical records of mercury stable isotopes in sediments of Tibetan lakes. Sci Rep 6, 23332.
Zheng, W., Hintelmann, H., 2009. Mercury isotope fractionation during photoreduction in natural water is controlled by its Hg/DOC ratio. Geochim. Cosmochim. Acta 73, 6704–6715.
Zhu, M.Y., Zhang, J.M., Steiner, M., Yang, A.H., Li, G.X., Erdtmann, B.D., 2003. Sinian-Cambrian stratigraphic framework for shallow- to deep-water environments of the Yangtze platform: an integrated approach. Prog. Nat. Sci. 13, 951–960.